Automated Soft Pressure Sensor Array-Based Sea Lamprey Detection Using Machine Learning

Hongyang Shi, *Member, IEEE*, Yu Mei, *Graduate Student Member, IEEE*, Ian González-Afanador, *Member, IEEE*, Claudia Chen, Scott Miehls, Christopher Holbrook, Nelson Sepúlveda, *Senior Member, IEEE*, and Xiaobo Tan, *Fellow, IEEE*

***Abstract*—Sea lamprey, a destructive invasive species in the Great Lakes in North America, is among very few fishes that rely on oral suction during migration and spawning. Recently, soft pressure sensors have been proposed to detect the attachment of sea lamprey as part of the monitoring and control effort. However, human decision is still required for the recognition of patterns in the measured signals. In this article, a novel automated soft pressure sensor array-based sea lamprey detection framework is proposed using object detection convolutional neural networks. First, the resistance measurements of the pressure sensor array are converted to mappings of relative change in resistance. These mappings typically show two different types of patterns under lamprey attachment: a high-pressure circular pattern corresponding to the mouth rim compressed against the sensor ("compression" pattern), and a low-pressure blob corresponding to the partial vacuum region of the sucking mouth ("suction" pattern). Three types of object detection algorithms, single-shot detector (SSD), RetinaNet, and YOLOv5s, are applied to the dataset of measurements collected in the presence of sea lamprey attachment, and the comparison of their performance shows that YOLOv5s model achieves the highest mean average precision (mAP) and the fastest inference speed. Furthermore, to improve the accuracy of the prediction model and reduce the false positive (FP) rate due to the sensor's memory effect, a filter branch with different detection thresholds for the compression and suction patterns, respectively, is added to the original machine-learning algorithm. The trained model is validated and used to automatically detect sea lamprey attachments and locate the suction area on the sensor in real time.**

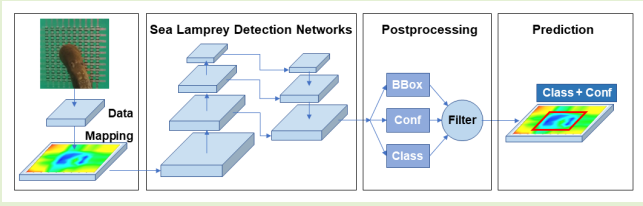

***Index Terms*—Invasive species monitoring, machine learning, sea lamprey detection, soft pressure sensor.**

I. Introduction

SEA lamprey (*Petromyzon marinus*) is a devastating, invasive fish species in the Laurentian Great Lakes of North America requiring a multimillion-dollar annual control program to protect native fish stocks. A single sea lamprey is capable of consuming 40 lb of host fish during its 12–16-month parasitic life stage [1]. Following the invasion, sea lampreys contributed to the collapse of native fish stocks and of a fishery currently valued at $4.5 billion annually [2]. A binational effort, lead by the Great Lakes Fishery Commission (GLFC), suppresses sea lamprey populations through the use of selective chemical applications [2] and migratory barriers [3], [4], and abundance is monitored through the capture of migratory adults [2]. Migratory barriers block not only invasive species, but desirable species and native species as well resulting in a desire for selective passage [5], [6] around migratory barriers for desirable species. Furthermore, maintaining a network of traps for assessment can be labor-intensive and costly. A means to autonomously detect and monitor sea lamprey could aid with the implementation of selective passage, design of new trapping or population assessment techniques, and help to understand their life history and ecology (e.g., refuge-seeking behavior and habitat characteristics).

New sensor technology that targets a unique aspect of sea lamprey biology and behavior may provide a solution for

Manuscript received 1 September 2022; revised 19 January 2023; accepted 21 January 2023. Date of publication 2 March 2023; date of current version 31 March 2023. This work was supported by the Great Lakes Fishery Commission under Grant 2022_TAN_541006. The associate editor coordinating the review of this article and approving it for publication was Prof. Dongsoo Har. *(Corresponding authors: Hongyang Shi; Xiaobo Tan.)*

This work involved human subjects or animals in its research. Approval of all ethical and experimental procedures and protocols was granted by Michigan State University's Institutional Animal Care and Use Committee (IACUC) under Application No. 02/18-028-00 and AMEND202200009/PROTO202100177.

Hongyang Shi, Yu Mei, Ian González-Afanador, Claudia Chen, Nelson Sepúlveda, and Xiaobo Tan are with the Department of Electrical and Computer Engineering, Michigan State University, East Lansing, MI 48824 USA (e-mail: shihong1@msu.edu; meiyu1@msu.edu; gonza834@msu.edu; chenclau@msu.edu; sepulve6@msu.edu; xbtan@egr.msu.edu).

Scott Miehls and Christopher Holbrook are with the U.S. Geological Survey, Great Lakes Science Center, Hammond Bay Biological Station, Millersburg, MI 49759 USA (e-mail: smiehls@usgs.gov; cholbrook@usgs.gov).

This article has supplementary downloadable material available at https://doi.org/10.1109/JSEN.2023.3249625, provided by the authors.

Digital Object Identifier 10.1109/JSEN.2023.3249625

automated detection. During upstream migration, the spawning phase adult sea lamprey will rest by attaching to smooth surfaces such as rocks or artificial walls (dams, fishways, and so on). They do so by creating negative pressure using their oral disk like a suction cup creating a unique pressure pattern. Pressure sensors paired with object detection technology may be used to detect that pattern and identify the pattern of sea lamprey attachment. Object detection is a technology for identifying instances of objects of a certain class in images, videos, and other types of datasets. It has numerous applications, such as number plate recognition [7], product identification [8], [9], face detection and recognition [10], animal monitoring [11], and autonomous driving [12]. Video analysis based on object detection methods has been used to detect underwater adult Pacific lampreys (*Entosphenus tridentatus*) [13]; however, image quality may not be suitable under a wide range of light conditions. Instead, underwater sea lampreys could be detected by taking advantage of their oral suction trait [14] in a more economical and efficient way using some proper pressure sensors [15], [16], [17] or contact sensors [18]. This is feasible since the suction of a sea lamprey's oral disk on the sensor would introduce distinct pressure patterns or related changes in the sensor's characteristics. Nevertheless, the sensor system alone significantly relies on human intervention to recognize the pressure patterns or contact events from the sensor's output signals and to further decide whether, when, and where the sea lamprey is attaching.

To reduce the burden of human decisions, the sea lamprey detection system needs to be automated. Before an automated solution is possible, an algorithm must be trained and tested to correctly identify the pressure pattern created by a sea lamprey attachment. This article reports the first automated sensing system for detecting sea lamprey attachment based on a soft pressure sensor array. Specifically, machine-learning-based object detection algorithms are used to learn features from the measured data of a soft pressure sensor array and perform automatic detection of sea lamprey attachment on the generated mapping contours.

In this article, a comprehensive sea lamprey mapping contour dataset is first generated for the training model to learn features. These mappings typically show two different types of patterns under lamprey attachment: a high-pressure circular pattern corresponding to the mouth rim compressed against the sensor ("compression" pattern) and a low-pressure blob corresponding to the partial vacuum region of the sucking mouth ("suction" pattern). Three types of object detection algorithms are deployed for sea lamprey detection, including single-shot detector (SSD) [19], RetinaNet [20], and YOLOv5s (which is a small-scale model of YOLOv5 [21] that has fewer layers of convolutional neural networks for faster and simpler object detection tasks). Their validation performance and inference speeds are evaluated and compared in-depth, and the results show that YOLOv5s achieves the highest mean average precision (mAP@0.5:0.95 up to 69.77%), and the fastest inference speed (up to 8.4 ms per image) on the experimental GPU device. Finally, a detection approach based on the YOLOv5s model with a confidence filter unit is proposed. In particular, different optimal detection thresholds are proposed for the compression and suction patterns, respectively, to reduce the false positive (FP) rate caused by the sensor's memory effect. The efficacy of the proposed method is supported by experimental results on real-time underwater detection of sea lampreys.

The rest of the article is structured as follows. Section II reviews the state-of-the-art object detection frameworks. Section III introduces the experimental animals and set up with the soft pressure sensor array. Section IV presents the sea lamprey dataset with its image annotation formats and shows the assessment results of three object detectors to find the best one. Then the sea lamprey detection approach with a postprocessing unit is proposed in Section V. Experimental results for evaluating the postprocessing performance are presented in Section VI. Concluding remarks are provided in Section VII.

II. Related Work

The state-of-the-art object detection algorithms can be categorized into two main types: one-stage and two-stage detectors. Representative two-stage object detectors are region-based convolutional neural networks (R-CNN [22], fast R-CNN [23], faster R-CNN [24], and mask R-CNN [25]), which first use selective search algorithms to extract candidate region proposals from the image and then classify every single object and estimate its size with a bounding box. They achieve higher detection accuracy but are typically slower than the one-stage detectors, which predict bounding boxes over the images without the region proposal step.

Examples of the most popular one-stage detectors include you only look once (YOLO) [26], SSD [19], and RetinaNet [20]. YOLO reframes object detection as a single regression problem from the image pixels to the bounding box coordinates and associated class probabilities. More advanced versions of YOLO have been released in the past few years, such as YOLOv3 [27], YOLOv4 [28], and YOLOv5 [21]. Different from all prior releases, YOLOv5 is implemented in PyTorch, which is well-supported on major platforms and is versatile for research prototyping. SSD uses a single deep neural network to output multiscale convolutional bounding box and predicts category scores and box offsets for a set of default bounding boxes. RetinaNet applies a modulating factor to the cross-entropy loss to address the extreme foreground–background class imbalance during training. However, RetinaNet still designs two separate subnetworks in the end: one for classifying anchor boxes, and the other for the regression of object boxes, which could be merged into one regression network in theory.

III. Experimental Animals and Setup

A. Experimental Animals

A total of 140 spawning phase adult sea lampreys were used to test on a 10-by-10 soft pressure sensor array during September 2021 ($n = 120$) and June 2022 ($n = 20$). Sea lampreys were captured in traps during upstream spawning migration in the St. Marys River (2021; Michigan, USA, and

Ontario, Canada) and the Cheboygan and Ocqueoc Rivers (2022; Michigan, USA). Sea lampreys were transported to Hammond Bay Biological Station (U.S. Geological Survey, Great Lakes Science Center, Millersburg, Michigan) and held in aerated, 1000-L flow-through tanks supplied continuously with Lake Huron water maintained at 8–12 °C until tests were conducted. All sea lamprey experiments were performed in accordance with protocols and guidelines approved by Michigan State University's Institutional Animal Care and Use Committee (IACUC, No. 02/18-028-00, and AMEND202200009/PROTO202100177). After the experiments in this study, the sea lampreys were housed for use in further research by Hammond Bay Biological Station staff.

B. Soft Pressure Sensor Array

As shown in Fig. 1(a), this work uses a 10-by-10 soft pressure sensor array (with a sensing area of 10×10 cm^2) that is made of piezoresistive films sandwiched between two layers of perpendicular copper tape electrodes, with polyester tape encapsulated on an acrylic plate. The detailed fabrication process is introduced in our previous work [15]. The sensor array forms a resistor network, with its circuits illustrated in Fig. 1(b).

At each sensor pixel, when a compressive pressure load is applied (e.g., under the compression of the lamprey mouth rim), the resistance at that pixel reduces, resulting in a reduction in the corresponding *measured* resistance via the coupling of the resistor network. Similarly, when a partial vacuum pressure (e.g., under the suction of the lamprey mouth) is applied on a sensor pixel, there will be a rise in the resistance measurement. The fabricated pressure sensor has a pressure sensing range between -10 and 235 kPa, and it has a sensitivity of -0.192 kPa^{-1} between 0 and 3 kPa, -0.016 kPa^{-1} between 3 and 28 kPa, and -0.002 kPa^{-1} between 28 and 50 kPa, respectively, as reported in our previous work [15]. It is observed that, likely due to the viscoelasticity of the films and their bonding, the resistance measurements do not immediately return to the at-rest values following the removal of the attachment. This memory effect, which would cause FPs in the detection, is explicitly addressed in the detection algorithm design.

C. Experimental Setup

As shown in Fig. 1(a), a voltage divider with a 1-kΩ reference resistor (R_{ref}) was used to measure the resistance of the pressure sensors at each pixel. An Arduino Mega 2560 microcontroller board provided a 5-V voltage supply (V_{cc}) for the pressure-sensing circuits and generated digital output signals for channel selection. Two analog/digital multiplexer breakout boards (SparkFun CD74HC4067, 16 channels) were used to choose the circuits between one column and one row of the perpendicular address lines. The output voltage (V_{out}) on the selected resistor network circuits was measured by a 10-bit analog-to-digital converter (ADC) through the analog input. The two-point resistance measurement R_j^k between the selected jth row and kth column can be calculated as follows:

$$R_j^k = \frac{V_{\text{out}}}{V_{\text{cc}} - V_{\text{out}}} R_{\text{ref}}. \tag{1}$$

The pressure-sensing panel was placed vertically along a glass wall of a 200-L water tank, while the microcontroller board and all other circuits were outside of the tank. The water level in the tank was about 5 cm higher than the top row electrode of the pressure sensing panel, submerging all the sensing areas.

In each round of measurement, the pressure-sensing system scanned the sensor array from the top left corner to the bottom right corner. Resistance was measured consecutively 20 times at each pressure sensor and then the average was taken as the measured two-point resistance at that pixel for that sampling cycle. The Arduino program repeated the scanning and measurement process every 1 s (1 Hz) in loops by means of a timer interrupt. The resistance measurement data were transferred to a Python program on a computer via serial communication and then the data would be stored as matrices in a spreadsheet file on the hard drive. Meanwhile, the relative change (in %) in the resistance matrix between the current sampling time and the initial value was calculated and converted to a mapping contour plot, which was also stored in the hard drive. Once the Arduino program started to run and measure the resistance periodically, an adult sea lamprey was transferred to the tank and introduced to attach to the sensing area for a certain time (e.g., >20 s). Resistance measurement lasted until the lamprey detached from the panel by itself or until the first 2 min of attachment elapsed.

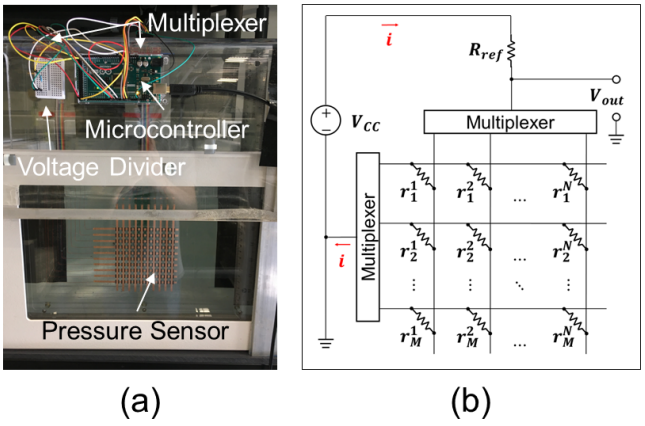

Fig. 1. Hardware of the soft pressure sensor array-based sea lamprey detection system [15]. (a) Experimental setup and (b) circuit model of the resistor network for the pressure sensor array.

IV. Training Models on the Sea Lamprey Dataset

This section first introduces the dataset collected from the sea lamprey experiments on the soft pressure sensor array, which are mapping contour plots converted from the resistance measurements. They can be categorized into either a "compression" pattern or a "suction" pattern. We present the image annotation formats for three object detection models: SSD, RetinaNet, and YOLOv5 and further implement the training

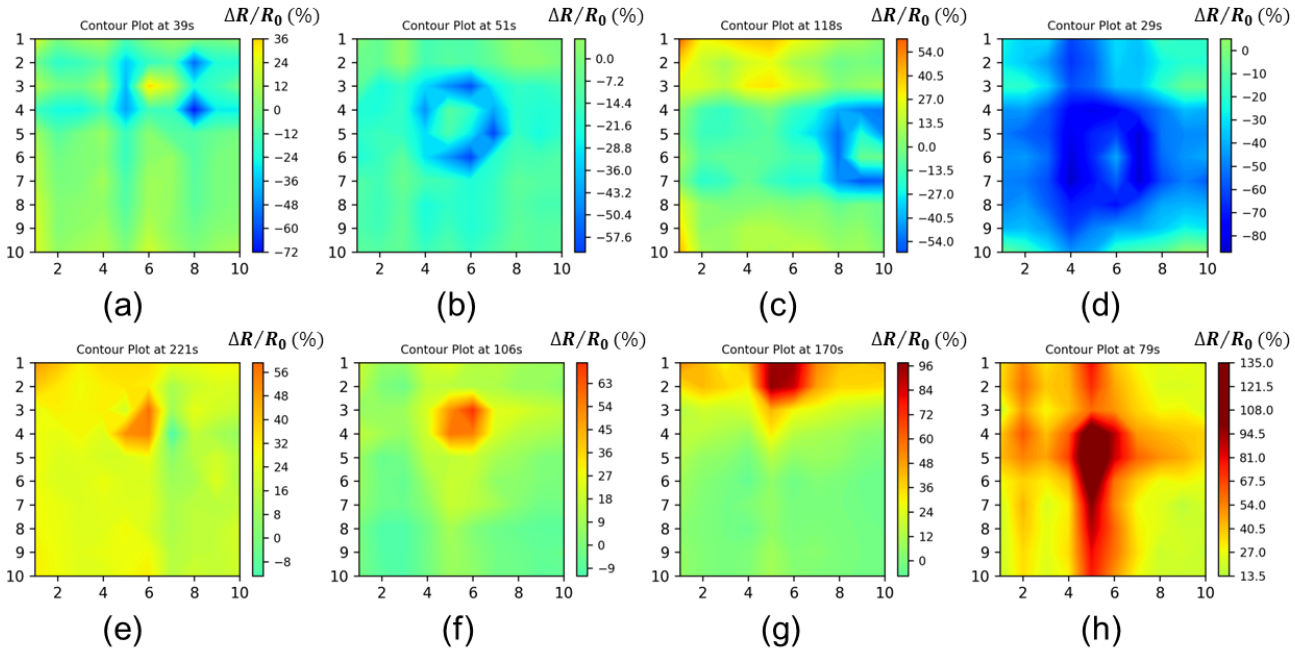

Fig. 2. Typical mapping contour plots of the 10-by-10 soft pressure sensor array with the attachment of an adult sea lamprey. Typical compression patterns: (a) with partial edges or points shown in blue reflecting compression of the lamprey's suction disk, (b) with a full circular pattern shown in blue, (c) with the compression area on the boundary of the sensing area, and (d) with a corrupted circular pattern connected to adjacent rows or columns due to crosstalk of the sensor array. Typical suction patterns: (e) with a triangular blob shown in red reflecting the suction area, (f) with an intact round (or octagon) blob shown in red, (g) with the suction area on the boundary of the sensing area, and (h) with a corrupted polygon pattern extended to adjacent rows or columns due to crosstalk of the sensor array.

and validation processes on each machine-learning model to find the best sea lamprey detector.

A. Mapping Contour Patterns

In this work, a total of 3094 colored mapping contour plots generated during the sea lamprey attachment periods were collected from 120 groups of sea lamprey experiments, which were annotated with bounding box labels for training and validating the neural networks. Each of these selected mapping contours had a resolution of 640 × 640 pixels and could be categorized into either a "compression" pattern or a "suction" pattern based on its overall appearance and contour levels. There were 623 compression plots and 2471 suction plots, and eight typical mapping contour plots are shown in Fig. 2, including four compression patterns [Fig. 2(a)–(d)] and four suction patterns [Fig. 2(e)–(h)]. For instance, the compression pattern can be partial edges or discrete points in blue [Fig. 2(a)] reflecting nonuniform compression of the lamprey's suction disk on the sensor array, a full circular pattern in blue [Fig. 2(b)], an arc in blue on the boundary [Fig. 2(c)], or a corrupted circular pattern connected to adjacent rows or columns [Fig. 2(d)] due to crosstalk of the sensor array. Similarly, the suction patterns are typically complementary to the compression patterns, which appear in red or orange blobs.

Note that, when a mapping contour plot displayed both a compression pattern and a suction pattern, such as Fig. 2(a), it would still be categorized into only one pattern with the higher magnitude in the absolute relative change in resistance. The annotated mapping contour dataset was then split into training and validation subsets with a ratio of 8:2.

On the other hand, a total of 3875 mapping contours obtained from the remaining 20 groups out of the whole 140 sea lamprey experiments were used to test the trained model with a postprocessing filter to decide the optimal confidence thresholds for the compression pattern and suction pattern, respectively.

B. Image Annotation

Fig. 3 shows an example of the annotation of the ground-truth bounding box on a suction pattern mapping contour. The coordinates of the ground-truth bounding box were obtained from the experimental videos synchronized with the pressure sensor measurements as follows. During the experiments, a cellphone camera was used to record activities on the whole sensor array. The mapping contour plots in a time sequence from a lamprey experiment were converted to an animation video. The animation contour video was then synchronized with the recorded experimental video. The video frames were extracted from the synchronized experimental video every 1 s, the same frame rate as that for the mapping contour animation video. Finally, the coordinates of the top left vertex (Col_{min}, Row_{min}) and the bottom right vertex (Col_{max}, Row_{max}) of the ground-truth bounding box were estimated with one decimal point between the boundary limits of 1.0 and 10.0.

Different object detectors may accept different formats of bounding box labels. The RetinaNet framework uses (class,

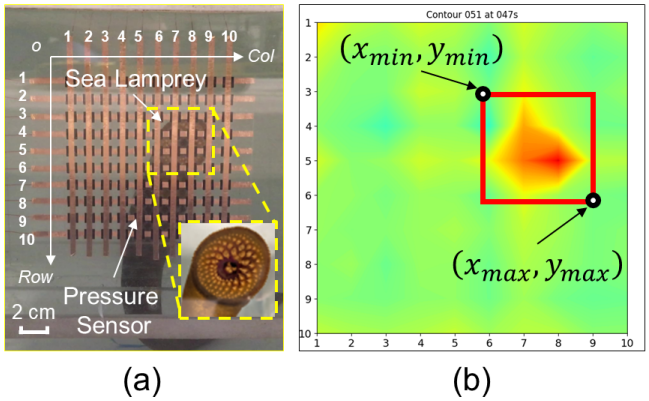

Fig. 3. Illustration of the ground-truth bounding box annotation. (a) Image of the 10-by-10 soft pressure sensor array under suction of an adult sea lamprey [15] (as shown in the inset), with the bounding box shown in yellow dashed lines covering the attachment area, and with the row and column axes labeled for dataset annotation. (b) Corresponding mapping contour plot of relative change in measured two-point resistance, with the ground-truth bounding box in red solid lines depicted on it.

$x_{\min}$, $y_{\min}$, $x_{\max}$, $y_{\max}$) as its label format, where class is either 0 or 1, which represents a "compression" or "suction" pattern, respectively; ($x_{\min}$, $y_{\min}$) denotes the pixel coordinates of the top left vertex, and ($x_{\max}$, $y_{\max}$) denotes those of the bottom right vertex, which can be obtained from the row and column coordinates

$$x_{\min} = \left(\frac{\mathrm{Col}_{\min} - 1}{10 - 1} \cdot r_w + r_{\mathrm{lm}}\right) \cdot \mathrm{Fig}_w \tag{2}$$

$$x_{\max} = \left(\frac{\mathrm{Col}_{\max} - 1}{10 - 1} \cdot r_w + r_{\mathrm{lm}}\right) \cdot \mathrm{Fig}_w \tag{3}$$

$$y_{\min} = \left(\frac{\mathrm{Row}_{\min} - 1}{10 - 1} \cdot r_h + r_{\mathrm{tm}}\right) \cdot \mathrm{Fig}_h \tag{4}$$

$$y_{\max} = \left(\frac{\mathrm{Row}_{\max} - 1}{10 - 1} \cdot r_h + r_{\mathrm{tm}}\right) \cdot \mathrm{Fig}_h \tag{5}$$

where the meanings of the parameters can be found in Table I.

On the other hand, in addition to the class label, the SSD and YOLOv5 object detection models take the normalized coordinates of the bounding box center (x_{center}, y_{center}), and the normalized width w_{bbox} and height h_{bbox} of the bounding box as accepted labels, and the formulas are given below

$$x_{\mathrm{center}} = \left(\frac{\frac{\mathrm{Col}_{\min} + \mathrm{Col}_{\max}}{2} - 1}{10 - 1} \cdot r_w + r_{\mathrm{lm}}\right) \tag{6}$$

$$y_{\mathrm{center}} = \left(\frac{\frac{\mathrm{Row}_{\min} + \mathrm{Row}_{\max}}{2} - 1}{10 - 1} \cdot r_h + r_{\mathrm{tm}}\right) \tag{7}$$

$$w_{\mathrm{bbox}} = \frac{\mathrm{Col}_{\max} - \mathrm{Col}_{\min} - 1}{10 - 1} \cdot r_w \tag{8}$$

$$h_{\mathrm{bbox}} = \frac{\mathrm{Row}_{\max} - \mathrm{Row}_{\min} - 1}{10 - 1} \cdot r_h. \tag{9}$$

C. Assessment of Three Object Detectors

The object detection frameworks, SSD, RetinaNet, and YOLOv5s, were evaluated for sea lamprey attachment pattern detection using the same training and validation datasets. The network hyperparameters for the training process, including the initial learning rate, momentum, weight decay, a minimum score threshold, and the nonmaximum suppression (NMS) [32] threshold, are chosen empirically using typical values that are used in common object detection networks, as listed in Table II. Here, the score threshold is the first filtering step to remove the very unlikely bounding boxes, while the NMS threshold is an evaluation metric to compare one candidate bounding box with multiple other bounding box candidates. The NMS is realized in this way: if they mutually share an IoU larger than the NMS threshold, then these bounding boxes could be merged into only one box with the maximum confidence score.

TABLE I
PARAMETERS FOR GENERATING THE MAPPING CONTOUR PLOTS

Name	Variable	Value
Figure width	Fig_w	640
Figure height	Fig_h	640
Ratio of contour width to figure width	r_w	0.9
Ratio of contour height to figure height	r_h	0.9
Ratio of contour left margin to figure width	r_{lm}	0.05
Ratio of contour top margin to figure height	r_{tm}	0.05
Colormap style	$cmap$	'jet'
Number of contour levels	N_{level}	100
Colorbar min limit	v_{min}	-100
Colorbar max limit	v_{max}	100

The training and validation process was implemented on the desktop PC with a GPU of NVIDIA GeForce RTX 3060 Ti (1.69 GHz boost clock) and 32.0 GB RAM. The input image of the mapping contours has a size of 640 × 640, without a colorbar plotted in it.

To quantitatively evaluate the validation performance, mAP is used, which is related to other performance metrics such as true positive (TP), FP, true negative (TN), false negative (FN), precision (P), recall (R), and average precision (AP). To decide whether a prediction is a TP or FP, the intersection over union (IoU) between the predicted and ground-truth bounding boxes, $\mathrm{IoU}_{\mathrm{pred}}^{g-t}$, was calculated. If $\mathrm{IoU}_{\mathrm{pred}}^{g-t} \geqslant \mathrm{IoU}$, then it is a TP, which means that the prediction as positive is correct; otherwise, it is regarded as an FP, meaning there was no object at that predicted place. Besides, FN means failing to predict an object that was actually there, and TN means the prediction as negative was true and there was indeed no object there. The corresponding TN rate, FP rate, TN rate, and FN rate are denoted as TPR, FPR, TNR, and FNR, respectively. The precision P represents the accuracy of the TN prediction among all the positive predictions, while the recall R depicts the percentage of TN prediction over all actual positives. They are calculated from the following formulas:

$$P = \frac{\mathrm{TPR}}{\mathrm{TPR} + \mathrm{FPR}} \tag{10}$$

$$R = \frac{\mathrm{TPR}}{\mathrm{TPR} + \mathrm{FNR}}. \tag{11}$$

Once the confidence scores of all predicted bounding boxes were obtained, the predictions were sorted in a descent order according to the confidence value. A few additional rounds

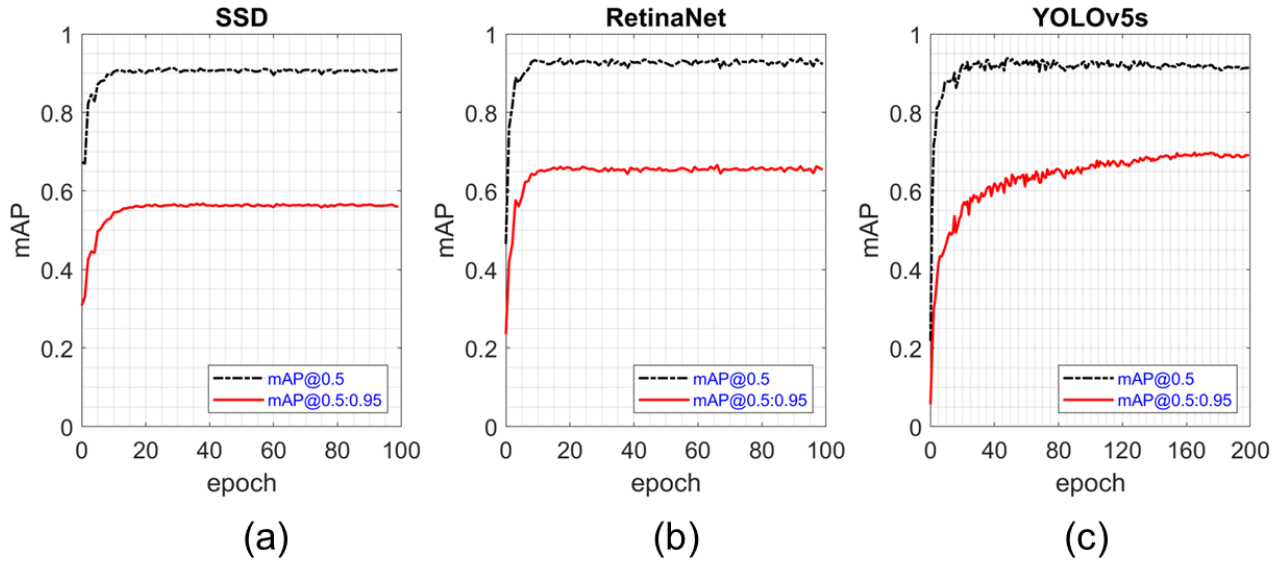

Fig. 4. Plots of mAP curves of different approaches in the validation process. (a) SSD, (b) RetinaNet, and (c) YOLOv5s.

TABLE II
HYPERPARAMETERS FOR TRAINING THE SEA LAMPREY DETECTION NETWORKS

Parameter	Value
Learning rate	0.005
Momentum	0.9
Weight decay	0.0005
Score threshold	0.05
NMS threshold	0.5

TABLE III
COMPARISON OF VALIDATION RESULTS OF DIFFERENT ALGORITHMS FOR SEA LAMPREY DETECTION

Framework	mAP(val)@0.5	mAP(val)@0.5:0.95	GPU Speed [ms / img]
SSD	90.79 %	56.81 %	11.4
RetinaNet	93.68 %	66.63 %	55.0
YOLOv5s	92.11 %	**69.77 %**	**8.4**

of performance evaluation were conducted. Specifically, each score was iteratively assigned as the IoU threshold to decide whether each prediction was a TP, FP, TN, or FN. And each new confidence-assigned IoU threshold resulted in a new precision value and a recall value, P and R, which could be used to plot the precision–recall curve. The average precision (AP) was then calculated as the area underneath the precision-recall curve

$$\mathrm{AP} = \int_0^1 P\,(R)\,dR. \tag{12}$$

And the mAP would be calculated by taking the mean AP over all classes and/or overall IoU thresholds. For instance, mAP@0.5 represents the mAP over all classes with an IoU threshold of 0.5 in the first round of deciding the prediction's performance, while mAP@0.5:0.95 has a similar meaning but it is further averaged over ten consecutive IoU thresholds from 0.5 to 0.95 with a step of 0.05.

The mAP curves are shown in Fig. 4 for SSD and RetinaNet after training for 100 epochs, and for YOLOv5s models after 200 epochs. The epoch numbers were selected differently to achieve the best and stable performance for each model. Particularly, the maximum values of mAP@0.5 and mAP@0.5:0.95 as well as the averaged GPU speed for image inference are listed in Table III. As can be seen, RetinaNet achieved the highest mAP@0.5 among all three models, 93.68%, compared to SSD's 90.79% and YOLOv5s' 92.11%. However, its maximum mAP@0.5:0.95 value was 66.63%, which was smaller than that of YOLOv5s, 69.77%. Basically, mAP@0.5:0.95 is a more comprehensive evaluation metric for object detection algorithms, as it takes multiple scales of IoU into consideration, which usually generates a more precise prediction. On the other hand, YOLOv5s cost the least inference time for each image, 8.4 ms on this GPU, which is qualified for future real-time sea lamprey detection applications. Therefore, YOLOv5s would be the best detector for this study.

V. FILTERED YOLOV5S FOR MITIGATION OF THE SENSOR MEMORY EFFECT

This section presents a real-time automated sea lamprey detection approach using an object detection method. As shown in Fig. 5, the proposed YOLOv5s model-based sea lamprey detection neural networks consists of three parts: a deep convolutional neural network backbone extracting feature maps from the input mapping contour image, a top-down architecture network neck constructing multiscale feature maps, and a confidence score filter end. The backbone and the neck can directly learn features from the measurements of a soft pressure sensor array and then predict the bounding box, class, and confidence of the input contour image. Meanwhile, due to the soft pressure sensor's memory effect, the detection network will view the leftover patterns following the detachment as a normal compression or suction

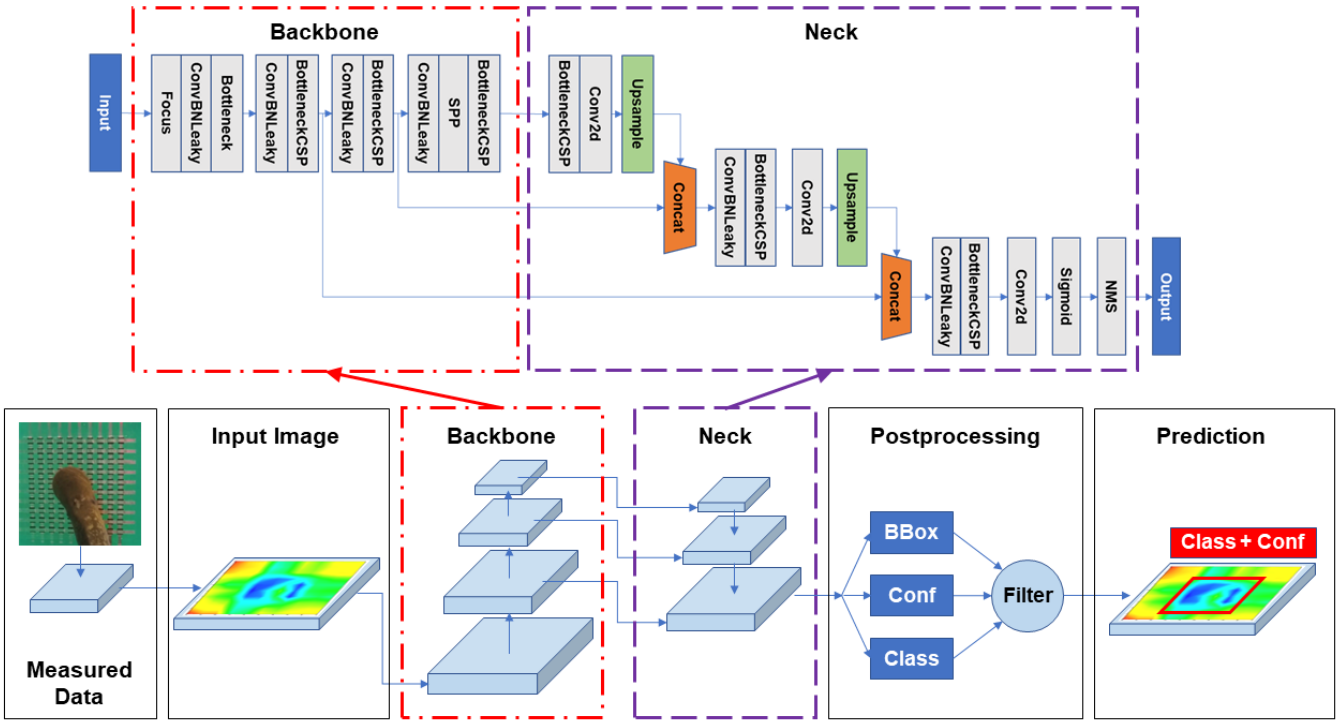

Fig. 5. Diagram of the soft pressure sensor and YOLOv5s model-based sea lamprey detection approach.

pattern, which could cause FPs in prediction. To mitigate such memory effect-induced faulty detection, a postprocessing head that filters the confidence of the compression pattern and suction pattern separately is added to the sea lamprey detection network. Each of the three aforementioned elements is elaborated on next.

A. Feature Learning Backbone and Neck of YOLOv5

As shown in the detailed diagram in Fig. 5, the feature learning networks of YOLOv5s mainly use three Bottleneck Cross Stage Partial (BottleneckCSP) Networks [29] as its backbone. The backbone first adopts a Focus layer [21] to slice the input images and reshape the dimensions, then four ConvBNLeaky modules are deployed interdigitatedly between the BottleneckCSP modules, each of which contains a convolution layer that is connected with a batch normalization (BN) layer and a LeakyReLU activation layer. After the last ConvBNLeaky layer, a spatial pyramid pooling (SPP) [30] module is used to remove the fixed-size constraint of the networks. The feature maps extracted from three levels of the backbone will be merged into the following neck part at three corresponding levels.

The feature fusion neck of YOLOv5s is constructed in a top-down feature pyramid network (FPN) [31] for building high-level semantic feature maps at all scales. These features are then enhanced with the features from the previous bottom-up pathway via lateral connections by concatenation, and the fused feature maps will be transferred to a ConvBNLeaky layer followed by another BottleneckCSP network and a basic 2-D convolution layer. The inference output will be sent to a sigmoid activation layer to regress the normalized bounding box center coordinates and the normalized widths and heights. Finally, an NMS [32] technique is applied to select the best bounding boxes from multiple candidates.

B. Postprocessing With Confidence Thresholds

After the feature fusion block, bounding box candidates of predicted sea lamprey attachment are obtained. Each of the valid candidates contains a pair of normalized center coordinates, a pair of normalized width and height, a class label, and a final confidence score. The confidence score is a probability that an object belongs to one class, which means the product of the object confidence Conf_{obj} and the class confidence Conf_{cls}. The object confidence is calculated from the IoU between the predicted bounding box and the ground-truth bounding box

$$\text{IoU}_{\text{pred}}^{g-t} = \frac{\text{Area of Intersection}}{\text{Area of Union}} \tag{13}$$

$$Pr_{\text{obj}} = \begin{cases} 0, & \text{if } \text{IoU}_{\text{pred}}^{g-t} = 0 \\ 1, & \text{otherwise} \end{cases} \tag{14}$$

$$\text{Conf}_{\text{obj}} = Pr_{\text{obj}} \cdot \text{IoU}_{\text{pred}}^{g-t}. \tag{15}$$

The class confidence is a conditional probability of the class when there is an object being predicted at that cell

$$\text{Conf}_{\text{cls}} = Pr_{\text{cls|obj}}. \tag{16}$$

So, the final confidence score can be written as follows:

$$\text{Conf} = \text{Conf}_{\text{cls}} \cdot \text{Conf}_{\text{obj}} = Pr_{\text{cls|obj}} \cdot Pr_{\text{obj}} \cdot \text{IoU}_{\text{pred}}^{g-t}. \tag{17}$$

The trained YOLOv5s model achieved good performance for the sea lamprey compression or suction pattern detection.

Nevertheless, faulty prediction of sea lamprey attachment was found in many lamprey experiments in the testing dataset. As discussed in Section III-B, the soft pressure sensor had some inherent memory effect when the compression was removed or when the suction pressure was released. Such a memory effect often lasted for more than 10 s after the lamprey detached from the sensor array. The overall memory effect showed a relatively low confidence score, thus it is promising to mitigate the false prediction by setting an additional postprocessing module with a higher threshold. Note that in most cases, the memory effect was more pronounced when the suction was removed than when the compression was removed from the sensor, which inspired us to set two different confidence thresholds for the compression pattern and the suction pattern, respectively.

The final confidence scores are fed into a confidence filter to remove all the bound box predictions with a confidence score less than a designed threshold. This filtering process proves to be effective for suppressing the sensor's memory effect as it only outputs the bounding box information at the beginning of the hardware's memory stage and prevents false detection in the remaining time. Two separate confidence thresholds (θ_C and θ_S) for the compression pattern and the suction pattern, respectively, are optimally selected, which will be discussed in Section VI. The output will be given according to the confidence value and the confidence threshold of that class

$$\text{Output} = \begin{cases} \text{BBox}_{\text{compression}}, & \text{if class = 0 and Conf} \geqslant \theta_C \\ \text{BBox}_{\text{suction}}, & \text{if class = 1 and Conf} \geqslant \theta_S \\ \text{None}, & \text{otherwise.} \end{cases} \tag{18}$$

VI. Results and Discussion

The testing dataset from the remaining 20 groups of sea lamprey experiments was used for testing the trained YOLOv5s model and getting class and confidence scores. Then the results with the ground-truth labels were investigated in-depth to find the optimal confidence thresholds that could not only improve the positive predictions, but also suppress FP predictions. We first split the testing output dataset into four groups: the true compression subset, the false compression subset, the true suction subset, and the false suction subset. For the compression subsets, a confidence threshold (θ_C) was set as a variable, changing from 0.05 to 1.0. According to this compression confidence threshold, the compression prediction dataset could be divided into four categories: TN compression (TPC), FP compression (FPC), TN compression (TNC), and FN compression (FNC). The corresponding TN rate, FP rate, TN rate, and FN rate for the compression pattern are noted as TPRC, FPRC, TNRC, and FNRC, respectively. In this way, the precision (P_C), recall (R_C), and the F-1 Score ($F1_C$) of the compression pattern could be evaluated as follows:

$$P_C(\theta_C) = \frac{\text{TPRC}(\theta_C)}{\text{TPRC}(\theta_C) + \text{FPRC}(\theta_C)} \tag{19}$$

$$R_C(\theta_C) = \frac{\text{TPRC}(\theta_C)}{\text{TPRC}(\theta_C) + \text{FNRC}(\theta_C)} \tag{20}$$

$$F1_C(\theta_C) = \frac{2 \cdot P_C(\theta_C) \cdot R_C(\theta_C)}{P_C(\theta_C) + R_C(\theta_C)}. \tag{21}$$

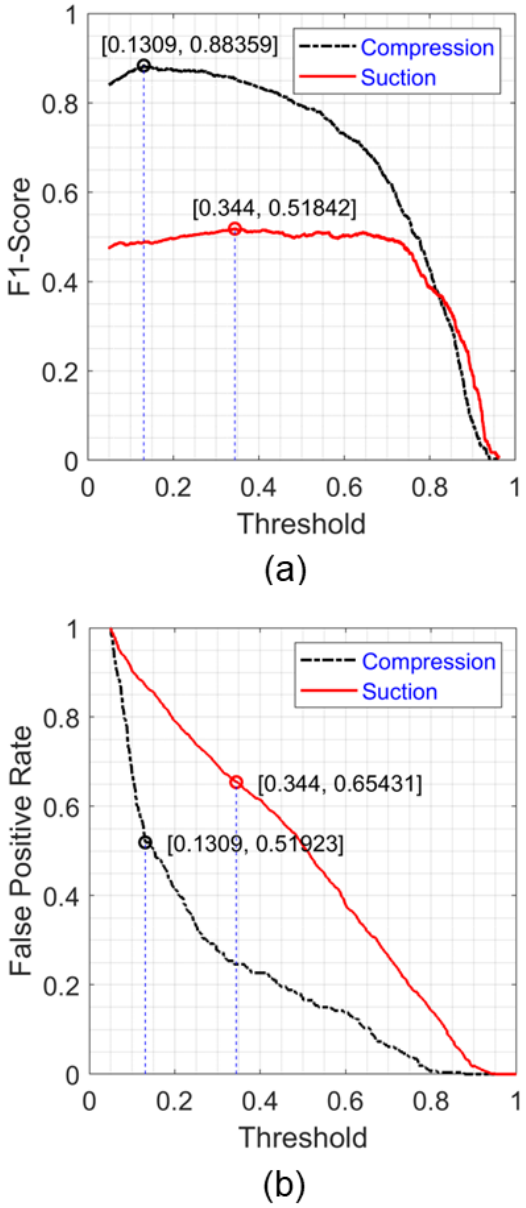

Fig. 6. Postprocessing results on the sea lamprey testing dataset with the confidence threshold as the variable. (a) F1-score curves and (b) FP rate curves, for both compression and suction patterns.

Here, F-1 score is a metric that balances the precision and the recall using their harmonic mean. The performance evaluation metrics for the suction pattern can be obtained similarly from the suction dataset. Then, the F-1 score curves of both compression and suction patterns can be drawn, as shown in Fig. 6(a). The maximum F-1 score is achieved as 0.88359 and 0.51842, when the confidence threshold is 0.1309 for the compression pattern, and 0.344 for the suction pattern, respectively.

In the meantime, the corresponding FP rate curves are shown in Fig. 6(b), which are directly related to the faulty detection due to the memory effect. As depicted in the figure, when the maximum F-1 score is achieved for the compression pattern and the suction pattern, respectively, the corresponding

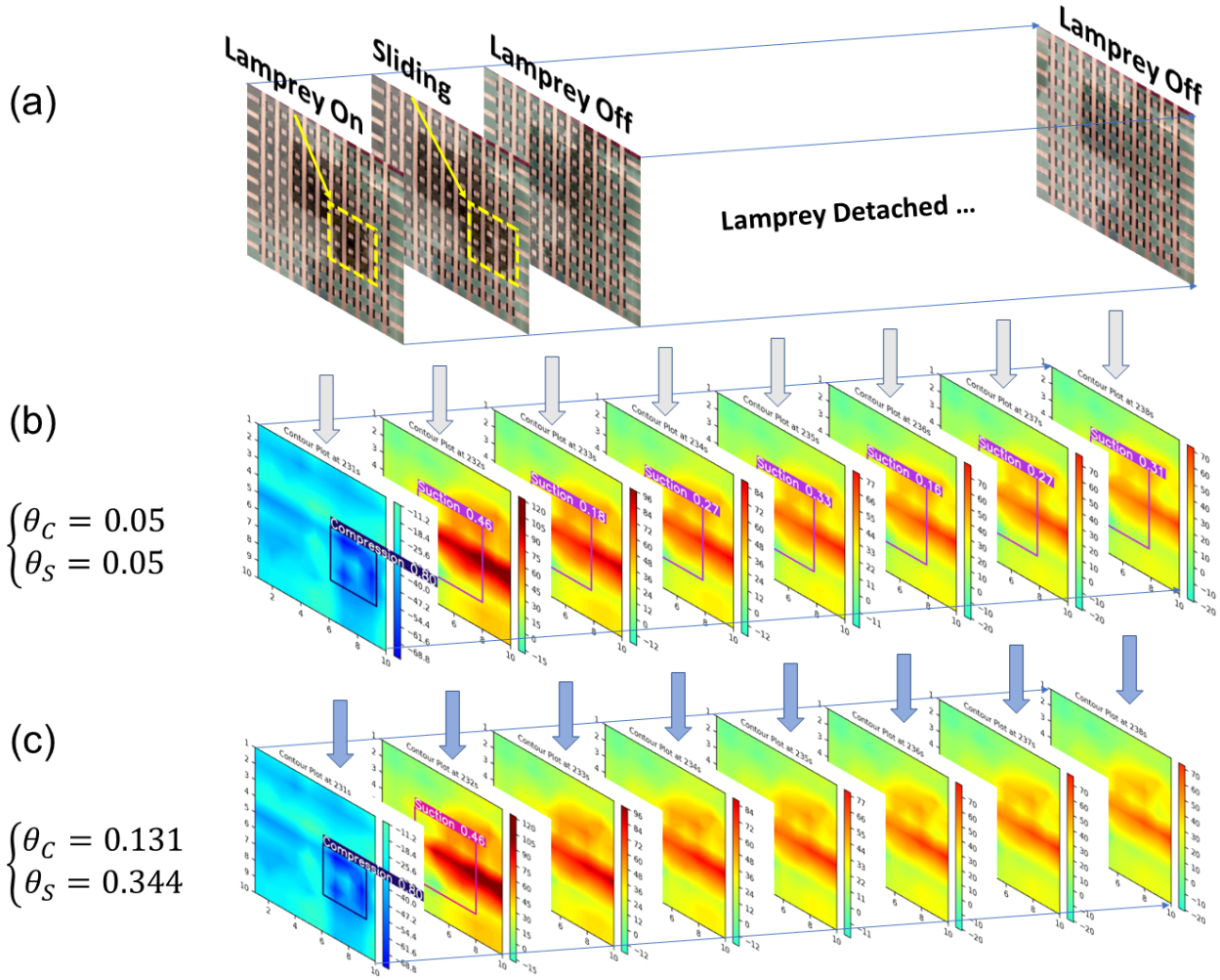

Fig. 7. Illustration of the faulty detection problem due to the sensor's memory effect. (a) Image sequence of the pressure sensor array with ground-truth bounding boxes. (b) Corresponding mapping contour plots with bounding box predictions from the YOLOv5s detection model without postprocessing (which means the confidence thresholds are both 0.05 for compression and suction patterns). (c) Filtered prediction results with a confidence threshold of 0.131 for the compression pattern and 0.344 for the suction pattern, respectively.

FP rate reaches 0.51923 and 0.65431, separately. Moreover, the higher the confidence threshold is, the lower the FP rate for both compression and suction patterns. However, this affects the F-1 score as well and would possibly reduce it when the threshold is too high. Therefore, we propose to take both the F-1 score and the FPR into consideration to determine a "tradeoff" between high positive prediction and low false prediction. This was realized by introducing a regularization coefficient to the following cost function:

$$L_C(\theta_C) = F1_C(\theta_C) - \lambda \cdot \mathrm{FPRC}(\theta_C) \tag{22}$$

where $\lambda \geqslant 0$ is the regularization (or penalty) parameter, which controls the relative importance of the F-1 score with regard to the regularization FPR term, and the subtract operation is used since higher F-1 score and lower FPR are desirable. The choice of the value of the regularization parameter λ can be determined by the specific purpose or focus of that application.

And the optimal confidence threshold $\hat{\theta}_C$ for the compression pattern was selected to maximize this cost function

$$\hat{\theta}_C = \arg\max_{\theta_C} L_C(\theta_C). \tag{23}$$

The cost function and the optimal confidence threshold for the suction pattern can be achieved similarly.

As an illustration, Fig. 7(a) shows a sequence of images from the recorded experimental video with ground-truth bounding box annotation, Fig. 7(b) shows the corresponding mapping contours with the original predictions from the YOLOv5s model, and Fig. 7(c) shows the corresponding mapping contours with the filtered predictions from the YOLOv5s model with two designed confidence thresholds. The corresponding predicted information for this time period is also listed in Table IV. At the first second ($t = 231$ s), a sea lamprey's mouth was attached on the right side of the sensor array, while the original prediction showed a correct compression pattern in Fig. 7(b). Then in the next second,

TABLE IV
PREDICTED INFORMATION DURING AN INTERVAL OF THE SENSOR'S MEMORY EFFECT

Time [s]	Class	Confidence	True or False
231	Compression	0.80	True
232	Suction	0.46	True
233	Suction	0.18	False
234	Suction	0.27	False
235	Suction	0.33	False
236	Suction	0.16	False
237	Suction	0.27	False
238	Suction	0.31	False

the sea lamprey slid to the right boundary and disengaged from the sensor array. The original predicted bounding box in Fig. 7(b) at this time instant did not track the sliding of the suction pattern to the right side. Moreover, in the following time interval (231–238 s), the lamprey had been completely away from the sensor array, but there were still suction patterns shown in the following mapping contours, and consequently, the original YOLOv5s detection network still plotted predicted bounding boxes on each contour in Fig. 7(b). On the contrary, when the confidence threshold was set as 0.131 for the compression pattern, and 0.344 for the suction pattern in the postprocessing unit (in this case, $\lambda = 0$), the filtered predictions turned out to be correct with most of the false prediction bounding boxes not displayed on the results. This filtering process with a pair of selected confidence thresholds proves to be simple but effective to soft pressure sensor array-based sea lamprey detection. To demonstrate the performance of the proposed method in a more visualized way, an animated contour video with the corresponding recorded sea lamprey experimental video is provided in the Supporting Video. In addition, as shown in the second part of the video, when the sea lamprey was housed in a perforated cage underwater at a depth of 24 in, where it could swim and explore freely by itself, our proposed method can still effectively detect the sea lamprey's attachment. This demonstrates the robustness of our sea lamprey detection system under various experimental conditions.

VII. CONCLUSION AND FUTURE WORK

Sea lamprey is a destructive invasive fish species in the Great Lakes, which has a specific oral suction trait that can be utilized for sea lamprey detection. This work introduced an automated soft pressure sensor array-based sea lamprey detection approach using object detection neural networks, with a designed confidence threshold to mitigate the sensor's memory effect before final prediction outputs. We first collected a comprehensive sea lamprey dataset of attachment mapping contours with two major patterns: "compression" and "suction" patterns and annotated the dataset with a ground-truth bounding box and class estimated from the synchronized experimental videos. Then three different object detection models were trained and validated on this sea lamprey dataset. By evaluating their overall performance, the YOLOv5s model was selected as our sea lamprey detection approach. More importantly, to achieve the best precision and suppress false prediction due to the sensor's memory effect, a postprocessing unit was added to the YOLOv5s model with two different confidence thresholds for the two categories of patterns. And the tradeoff between higher precision and lower FP rate could be achieved by a regularization method.

For future work, we will develop soft pressure sensor arrays with larger sensing areas and higher spatial resolution on soft and nonflat substrates and test our automated sea lamprey detection approach on these sensors. The hyperparameters for training the sea lamprey detection networks will also be tuned to find optimized values. Furthermore, the developed automated lamprey detection system will be experimentally tested in the field environment, to evaluate its performance and robustness in the presence of practical challenges such as flow disturbances and variations in ambient temperatures. On the other hand, although the filter unit added to this sea lamprey detection system has been proven to be simple and efficient for mitigation of the sensor's memory effect, the mapping contour images are processed frame by frame individually according to the output confidence, and the sea lamprey's suction dynamics has not been taken into consideration, which leads to decreasing intensity of patterns and may create potential problems such as missing detected pattern that includes actual attachment instance (i.e., FN prediction). Therefore, an alternative way to mitigate the sensor's memory effect might be looking into the time-series data of the output class and confidence and even the bounding box coordinates. By developing another recurrent neural network (RNN) as the postprocessing unit to learn from these time series data, the sea lamprey's suction dynamics such as the varying trend of the mapping contour patterns between the attachment and detachment events is possible to be captured, thus a more robust detection might be achieved. In addition to RNNs, a simpler approach for future investigation could include using a window of snapshots instead of a single snapshot to extract the trend in the patterns.

ACKNOWLEDGMENT

The authors thank Trisha Searcy, Riley Waterman, and Frank Bajenske for their great assistance in the lamprey experiments. They also thank Jacob Blatt for his help in the initial image annotation. Any use of trade, product, or firm names is for descriptive purposes only and does not imply endorsement by the US Government.

REFERENCES

[1] W. D. Swink, "Host selection and lethality of attacks by sea lampreys (Petromyzon marinus) in laboratory studies," *J. Great Lakes Res.*, vol. 29, pp. 307–319, Jan. 2003.

[2] J. E. Marsden and M. J. Siefkes, "Control of invasive sea lamprey in the Great Lakes, Lake Champlain, and Finger Lakes of New York," in *Lampreys: Biology, Conservation and Control*, vol. 2, J. Margaret and F. Docker, Ed. Corvallis, OR, USA: McGraw-Hill, 2019, pp. 411–479.

[3] R. L. McLaughlin, A. Hallett, T. C. Pratt, L. M. O'Connor, and D. G. McDonald, "Research to guide use of barriers, traps, and fishways to control sea lamprey," *J. Great Lakes Res.*, vol. 33, pp. 19–37, Jan. 2007.

[4] H. R. Dodd et al., "Low-head sea lamprey barrier effects on stream habitat and fish communities in the Great Lakes basin," *J. Great Lakes Res.*, vol. 29, pp. 386–402, Jan. 2003.

[5] T. C. Pratt et al., "Balancing aquatic habitat fragmentation and control of invasive species: Enhancing selective fish passage at sea lamprey control barriers," *Trans. Amer. Fisheries Soc.*, vol. 138, no. 3, pp. 652–665, 2009.

[6] R. L. McLaughlin et al., "Unintended consequences and trade-offs of fish passage," *Fish Fisheries*, vol. 14, no. 4, pp. 580–604, 2013.

[7] R.-C. Chen, "Automatic license plate recognition via sliding-window darknet-YOLO deep learning," *Image Vis. Comput.*, vol. 87, pp. 47–56, Jul. 2019.

[8] P. Chu, Z. Li, K. Lammers, R. Lu, and X. Liu, "Deep learning-based apple detection using a suppression mask R-CNN," *Pattern Recognit. Lett.*, vol. 147, pp. 206–211, Jul. 2021.

[9] L. Tan, T. Huangfu, L. Wu, and W. Chen, "Comparison of RetinaNet, SSD, and YOLO v3 for real-time pill identification," *BMC Med. Informat. Decis. Making*, vol. 21, no. 1, pp. 1–11, Dec. 2021.

[10] G. Guo and N. Zhang, "A survey on deep learning based face recognition," *Comput. Vis. Image Understand.*, vol. 189, Dec. 2019, Art. no. 102805.

[11] J. Zhong, M. Li, J. Qin, Y. Cui, K. Yang, and H. Zhang, "Real-time marine animal detection using YOLO-based deep learning networks in the coral reef ecosystem," in *Proc. 7th Int. Conf. Ubiquitous Positioning, Indoor Navigat. Location-Based Services (UPINLBS)*, Wuhan, China, 2022, pp. 301–306.

[12] D. Feng et al., "Deep multi-modal object detection and semantic segmentation for autonomous driving: Datasets, methods, and challenges," *IEEE Trans. Intell. Transp. Syst.*, vol. 22, no. 3, pp. 1341–1360, Mar. 2021.

[13] C. Negrea, D. E. Thompson, S. D. Juhnke, D. S. Fryer, and F. J. Loge, "Automated detection and tracking of adult Pacific lampreys in underwater video collected at snake and Columbia river fishways," *North Amer. J. Fisheries Manage.*, vol. 34, no. 1, pp. 111–118, Feb. 2014.

[14] H. Shi, C. M. Holbrook, Y. Cao, N. Sepúlveda, and X. Tan, "Measurement of suction pressure dynamics of sea lampreys, petromyzon marinus," *PLoS ONE*, vol. 16, no. 4, Apr. 2021, Art. no. e0247884.

[15] H. Shi, I. Gonzalez-Afanador, C. Holbrook, N. Sepulveda, and X. Tan, "Soft pressure sensor for underwater sea lamprey detection," *IEEE Sensors J.*, vol. 22, no. 10, pp. 9932–9944, May 2022.

[16] Y. Cao, H. Shi, X. Tan, and N. Sepúlveda, "Enabling negative pressure sensing through ferroelectret device," *IEEE Sensors Lett.*, vol. 6, no. 8, pp. 1–4, Aug. 2022.

[17] Y. Cao, H. Shi, X. Tan, and N. Sepúlveda, "Nanogenerator-based bidirectional pressure sensor array and its demonstration in underwater invasive species detection," *Nano Res.*, Nov. 2022.

[18] I. Gonzalez-Afanador, H. Shi, C. Holbrook, X. Tan, and N. Sepúlveda, "Invasive sea lamprey detection and characterization using interdigitated electrode (IDE) contact sensor," *IEEE Sensors J.*, vol. 21, no. 24, pp. 27947–27956, Dec. 2021.

[19] W. Liu et al., "SSD: Single shot multibox detector," in *Proc. Eur. Conf. Comput. Vis. (ECCV)*, vol. 9905, 2016, pp. 21–37.

[20] T.-Y. Lin, P. Goyal, R. Girshick, K. He, and P. Dollár, "Focal loss for dense object detection," in *Proc. IEEE Int. Conf. Comput. Vis. (ICCV)*, Oct. 2017, pp. 2980–2988.

[21] G. Jocher et al., "Ultralytics/YOLOv5: V3.1—Bug fixes and performance improvements," Zenodo, Tech. Rep., 2020, doi: 10.5281/zenodo.4154370.

[22] R. Girshick, J. Donahue, T. Darrell, and J. Malik, "Rich feature hierarchies for accurate object detection and semantic segmentation," in *Proc. IEEE Conf. Comput. Vis. Pattern Recognit.*, Jun. 2014, pp. 580–587.

[23] R. Girshick, "Fast R-CNN," in *Proc. IEEE Int. Conf. Comput. Vis. (ICCV)*, Dec. 2015, pp. 1440–1448.

[24] S. Ren, K. He, R. Girshick, and J. Sun, "Faster R-CNN: Towards real-time object detection with region proposal networks," in *Proc. Adv. Neural Inf. Process. Syst. (NIPS)*, 2015, pp. 1–9.

[25] K. He, G. Gkioxari, P. Dollár, and R. Girshick, "Mask R-CNN," in *Proc. IEEE Int. Conf. Comput. Vis. (ICCV)*, 2017, pp. 2961–2969.

[26] J. Redmon et al., "You only look once: Unified, real-time object detection," in *Proc. IEEE Conf. Comput. Vis. Pattern Recognit. (CVPR)*, Jun. 2016, pp. 779–788.

[27] J. Redmon and A. Farhadi, "YOLOv3: An incremental improvement," 2018, *arXiv:1804.02767*.

[28] A. Bochkovskiy, C.-Y. Wang, and H.-Y. Mark Liao, "YOLOv4: Optimal speed and accuracy of object detection," 2020, *arXiv:2004.10934*.

[29] C.-Y. Wang, H.-Y. Mark Liao, Y.-H. Wu, P.-Y. Chen, J.-W. Hsieh, and I.-H. Yeh, "CSPNet: A new backbone that can enhance learning capability of CNN," in *Proc. IEEE/CVF Conf. Comput. Vis. Pattern Recognit. Workshops (CVPRW)*, Jun. 2020, pp. 1571–1580.

[30] K. He, X. Zhang, S. Ren, and J. Sun, "Spatial pyramid pooling in deep convolutional networks for visual recognition," *IEEE Trans. Pattern Anal. Mach. Intell.*, vol. 37, no. 9, pp. 1904–1916, Sep. 2014.

[31] T.-Y. Lin, P. Dollár, R. Girshick, K. He, B. Hariharan, and S. Belongie, "Feature pyramid networks for object detection," in *Proc. IEEE Conf. Comput. Vis. Pattern Recognit. (CVPR)*, Jul. 2017, pp. 2117–2125.

[32] A. Neubeck and L. Van Gool, "Efficient non-maximum suppression," in *Proc. 18th Int. Conf. Pattern Recognit. (ICPR)*, Aug. 2006, pp. 850–855.

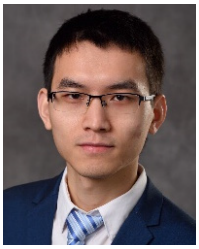

Hongyang Shi (Member, IEEE) received the B.S. degree in mechanical design, manufacturing, and automation and the M.S. degree in mechatronics engineering from the Huazhong University of Science and Technology (HUST), Wuhan, China, in 2012 and 2015, respectively, and the Ph.D. degree in electrical and computer engineering from Michigan State University (MSU), East Lansing, MI, USA, in 2022.

He is currently a Postdoctoral Researcher in the Department of Aerospace Engineering and Engineering Mechanics, University of Texas, Austin, TX, USA. His research interests include soft robotics and haptic sensing.

Dr. Shi was a recipient of the China National Scholarship in 2010, the China National Endeavor Fellowship in 2011, the FESTO Scholarship in 2012 from HUST, the MSU Engineering Distinguished Fellowship in 2016, the Graduate Office Fellowship in 2018, the Dissertation Completion Fellowship in 2021, and the Fitch H. Beach Award 3rd place, in 2022 from the College of Engineering at MSU.

Yu Mei (Graduate Student Member, IEEE) received the B.S. degree in robotics engineering from the School of Automation, Southeast University (SEU), Nanjing, China, in 2020. He is currently pursuing the Ph.D. degree in electrical and computer engineering with Michigan State University (MSU), East Lansing, MI, USA.

His research interests include modeling and control in robotics, soft robotics, rehabilitation robots, and pattern recognition.

Dr. Mei was a recipient of the Outstanding Graduate Award from the School of Automation at SEU in 2020 and the Engineering Distinguished Scholar Award in 2021 from MSU.

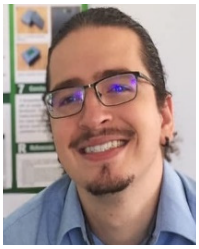

Ian González-Afanador (Member, IEEE) received the B.S. degree in electrical and computer engineering from the University of Puerto Rico, Mayagüez, Puerto Rico, in 2019. He is currently pursuing the Ph.D. degree in electrical and computer engineering with Michigan State University, East Lansing, MI, USA.

He has internships with Honeywell Aerospace and Lockheed-Martin Sikorsky, Stratford, CT, USA. He has participated in summer research programs at the University of Virginia, Charlottesville, VA, USA, Michigan State University, and Georgia Tech, Atlanta, GA, USA. His current research focuses on the development of underwater biological contact/accumulation and the development of piezoelectric-based antifouling systems for light sources used in algal cultivation.

Dr. González-Afanador was a recipient of the NSF Graduate Research Fellowship and the MSU University Distinguished Fellowship.

Claudia Chen received the B.S. degree in mechanical engineering from Michigan State University (MSU), East Lansing, MI, USA, in 2022, and where she is currently pursuing the Ph.D. degree in electrical and computer engineering.

She has participated in a summer research program at Georgia Tech, Atlanta, GA, USA. Her research interests include soft robotics and sensors. Her current research focuses on the development of piezoresistive pressure sensor arrays.

Scott Miehls is a Research Fishery Biologist at the Great Lakes Science Center's Hammond Bay Biological Station, Millersburg, MI, USA. He is the Principal Investigator for multiple projects focused on understanding the behavior and biology of the invasive sea lamprey in the Great Lakes, the development of invasive species control measures, and the development of fish passage tools to improve connectivity for native Great Lakes fish species between the lakes and their tributaries. His research interests include understanding the biology and the behavior of both native and invasive species and working with management agencies to develop tools for improving fisheries science and management in the Great Lakes.

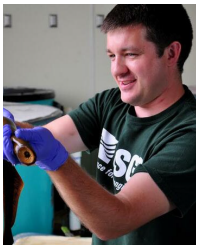

Christopher Holbrook received the B.S. and M.S. degrees in zoology from the University of Maine, Orono, ME, USA, in 2004 and 2007, respectively, and the Ph.D. degree in fisheries and wildlife from Michigan State University, East Lansing, MI, USA, in 2015.

He is a Research Fishery Biologist at the Great Lakes Science Center's Hammond Bay Biological Station, Millersburg, MI. His research supports native fish restoration and fishery management in the Laurentian Great Lakes.

Nelson Sepúlveda (Senior Member, IEEE) received the B.S. degree in electrical and computer engineering from the University of Puerto Rico, Mayagüez, Puerto Rico, in 2001, and the M.S. and Ph.D. degrees in electrical and computer engineering from Michigan State University (MSU), East Lansing, MI, USA, in 2002 and 2005, respectively.

During the last year of graduate school, he attended the Sandia National Laboratories. In 2006, he joined as a Faculty Member with the Department of Electrical and Computer Engineering, University of Puerto Rico. He was a Visiting Faculty Researcher at the Air Force Research Laboratories, Dayton, OH, USA, in 2006, 2007, 2013, and 2014, the National Nanotechnology Infrastructure Network, in 2008, and the Cornell Center for Materials Research, Ithaca, NY, USA, in 2009; the last two being the National Science Foundation (NSF) funded centers at Cornell University, Ithaca, NY, USA. In 2011, he joined as a Faculty Member with the Department of Electrical and Computer Engineering, MSU, where he is currently a Professor. His current research interests include smart materials and the integration of such in microelectromechanical systems, with particular emphasis on vanadium dioxide thin films and the use of the structural phase transition for the development of smart microactuators.

Dr. Sepúlveda has received the NSF CAREER Award in 2010 and the MSU Teacher Scholar Award in 2015.

Xiaobo Tan (Fellow, IEEE) received the B.Eng. and M.Eng. degrees in automatic control from Tsinghua University, Beijing, China, in 1995 and 1998, respectively, and the Ph.D. degree in electrical and computer engineering from the University of Maryland, College Park, MD, USA, in 2002.

He is currently an MSU Foundation Professor and the Richard M. Hong Endowed Chair with the Electrical and Computer Engineering, Michigan State University (MSU), East Lansing, MI, USA. He has published over 300 papers and has been awarded four U.S. patents in these areas. His research interests include modeling and control of systems with hysteresis, electroactive polymer sensors and actuators, soft robotics, and bio-inspired underwater robots and their application to environmental sensing.

He is a Fellow of ASME. He was a recipient of the NSF CAREER Award in 2006, the MSU Teacher-Scholar Award in 2010, the MSU College of Engineering Withrow Distinguished Scholar Award in 2018, the Distinguished Alumni Award from the Department of Electrical and Computer Engineering at the University of Maryland in 2018, and multiple best paper awards. He has served as a Senior Editor for IEEE/ASME TRANSACTIONS ON MECHATRONICS.